ACS Energy LETTERS

Cite This: ACS Energy Lett. 2018, 3, 2232−2239

http://pubs.acs.org/journal/aelccp

LETTER

# Unconventional Relation between Charge Transport and Photocurrent via Boosting Small Polaron Hopping for Photoelectrochemical Water Splitting

Wenrui Zhang,[†] Feng Wu,[‡] Jun Li,[§] Danhua Yan,[†] Jing Tao,[§] Yuan Ping,[‡] and Mingzhao Liu*,[†]

[†]Center for Functional Nanomaterials, Brookhaven National Laboratory, Upton, New York 11973, United States

[‡]Department of Chemistry and Biochemistry, University of California, Santa Cruz, California 95064, United States

[§]Condensed Matter Physics and Materials Science Department, Brookhaven National Laboratory, Upton, New York 11973, United States

Supporting Information

**ABSTRACT:** Doping in semiconductor photoelectrodes controls defect formation and carrier transport that critically determine the device performance. Here we report an unconventional carrier transport relation that is tuned by extrinsic molybdenum (Mo) doping in $BiVO_4$ photoanodes. Using the single-crystalline thin film approach, we identify that Mo doping significantly condenses the optimization regime between carrier transport and photon collection. For Mo-doped $BiVO_4$ films, an unprecedentedly thin layer (50 nm), less than one-third of the pristine $BiVO_4$ thickness, delivers larger photocurrents by overcoming the charge transport limitation, representing a regime not covered in conventional models. We provide direct evidence that Mo doping improves electron transport by boosting not only the donor density but also the electron mobility in the form of a small polaron, with the latter applying substantial impact on the photoelectrochemical performance. Density functional theory calculations reveal that fully ionized Mo dopants establish a strong electrostatic interaction with a small polaron, which helps reduce its hopping barrier by minimizing the local lattice expansion. Our results deliver mechanistic insights on the interplay between extrinsic doping and carrier transport, and provide guidance in developing advanced semiconductor photoelectrodes.

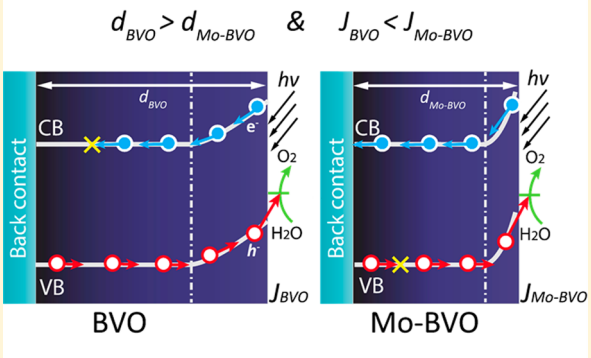


Doping semiconductors with selected impurities enables flexible modulation of fundamental physical properties and receives various applications in developing electronic, magnetic, and photonic devices such as transistors,[1,2] multiferroics,[3] nonvolatile memories,[4] solar cells,[5,6] and photoelectrodes for solar water splitting.[7,8] In semiconductor photoelectrodes, the doping strategy using native nonstoichiometric vacancies[9] or extrinsic impurities[10] has been intensively exploited to enhance light absorption or to improve carrier transport for optimized device efficiency. In particular, doping bismuth vanadate ($BiVO_4$, BVO) with hexavalent ions, such as molybdenum (Mo) or tungsten (W), is suggested to facilitate electron transport for improved photoelectrochemical (PEC) activity.[11−13] As one of the state-of-the-art photoanode materials, BVO possesses a moderate band gap of 2.4−2.6 eV for visible light absorption, appropriate valence band edges, relatively long hole diffusion length, and reasonable surface activity for water oxidation.[14−19] Despite its n-type conductivity nature, BVO suffers from poor electron transport, which is reflected from the highly insulating behavior and the larger back-illuminated photocurrent.[14,15] As such, the improvement to PEC performance achieved from hexavalent ion doping in BVO is conventionally attributed to the increased electron density. However, it is noted that very large variation is found in previous studies for both the optimized dopant concentration (0.15−3% atom ratio for Mo-BVO) and film thickness (120−1000 nm),[16−19] which is likely due to the variation in sample morphology and grain structures and makes the analysis highly convoluted. Therefore, it is very

Received: August 7, 2018
Accepted: August 27, 2018
Published: August 27, 2018






DOI: 10.1021/acsenergylett.8b01445
ACS Energy Lett. 2018, 3, 2232−2239

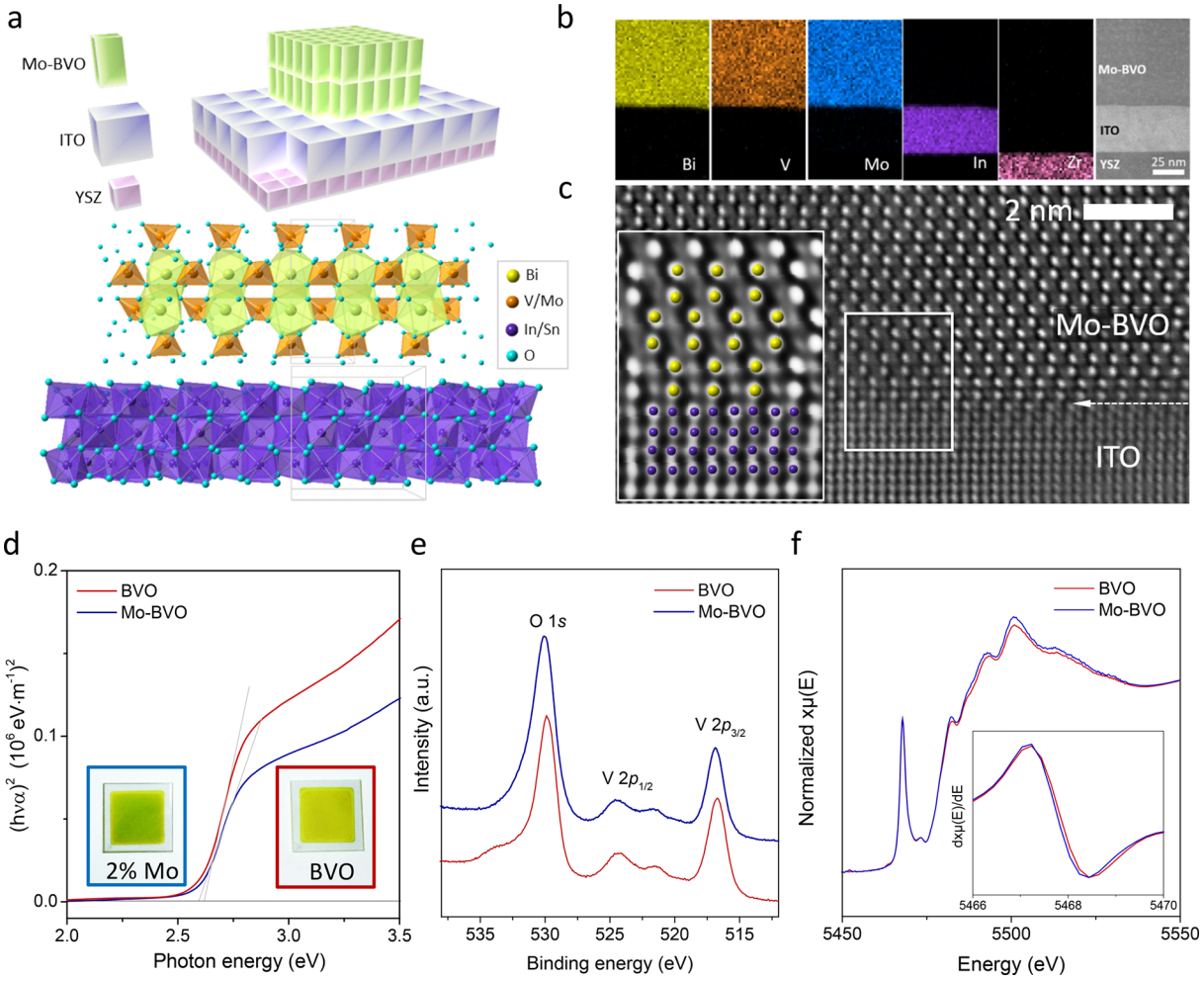


**Figure 1. (a) Schematic device structure and crystallographic model of single-crystalline Mo-BVO films over ITO/YSZ substrates. (b) Cross-sectional EDX mapping and corresponding HAADF-STEM image of a 2% Mo-BVO/ITO/YSZ heterostructure. (c) High-resolution STEM image of the Mo-BVO/ITO interface region demonstrating crystalline growth of BVO and ITO. The inset shows the lattice-matched BVO/ITO interface. (d) Tauc plots of 160 nm thick pristine BVO and 2% Mo-BVO films over ITO/YSZ determining their optical band gaps. The insets are the optical images of pristine BVO (right) and 2% Mo-BVO (left) films. (e) High-resolution XPS spectra of V 2p and O 1s core levels of pristine BVO and 2% Mo-BVO films. (f) X-ray absorption near-edge structure of pristine BVO and 10% Mo-BVO films collected at the V K-edge. The inset shows their first-derivative spectra identifying the edge shift at the V K-edge.**

challenging to generalize the fundamental doping mechanism from these studies.

Here, for the first time, we apply the single-crystalline thin film approach to the model system of Mo-doped BVO (Mo-BVO) to systematically assess the role of dopants in modulating carrier transport and resultant photocurrents. The single-crystalline Mo-BVO thin film provides a well-defined platform that allows precise control of doping concentration and film thickness with minimal morphology variation. As determined from combined solid-state transport and PEC measurements, the Mo doping not only increases the donor density but also lowers the small polaron hopping barrier. The latter effect is particularly significant but had not been fully recognized in previous studies. Due to the lowered small polaron hopping barrier, Mo-doping at low levels significantly improves electron transport with relatively minor penalty to hole transport. As a result, an unprecedentedly thin Mo-doped BVO photoelectrode (50 nm thick) already delivers larger photocurrents than a 160 nm thick pristine BVO, despite the lower photon collection. This phenomenon represents a situation that is beyond the scope of the conventional Gartner or Reichmann models, in which majority carrier transport is not limited. The origin of reduced small polaron mobility by Mo doping is further elucidated by density functional theory (DFT) calculations, which provide insights in developing dopants to modulate carrier transport and PEC performance.

*Doping Effect on Structural Distortion and Chemical Evolution.* The single-crystalline Mo-BVO films are prepared by pulsed laser deposition (PLD) over an indium tin oxide (ITO)-buffered yttria-stabilized cubic zirconia (YSZ) (001) substrate (Figure 1a). For such doped films, the dopant concentration in the form of $BiV_{1-x}Mo_xO_4$ is controlled from a very low level (0.01%) to a moderately high level (10%), with the latter one approaching the Mo solubility in the Bi−Mo−V−O ternary phase system.[20,21] The film morphology and surface roughness are similar for different doping levels (Figure S1), which is essential to minimize their effects on the photoelectrode performance. As a representative planar thin film heterostructure, the cross-sectional scanning transmission electron microscopy (STEM) image of the 2% Mo-BVO film is presented in Figure S2a. The phase purity and crystallinity are confirmed by selected area electron diffraction (SAED, Figure



DOI: 10.1021/acsenergylett.8b01445
ACS Energy Lett. 2018, 3, 2232−2239

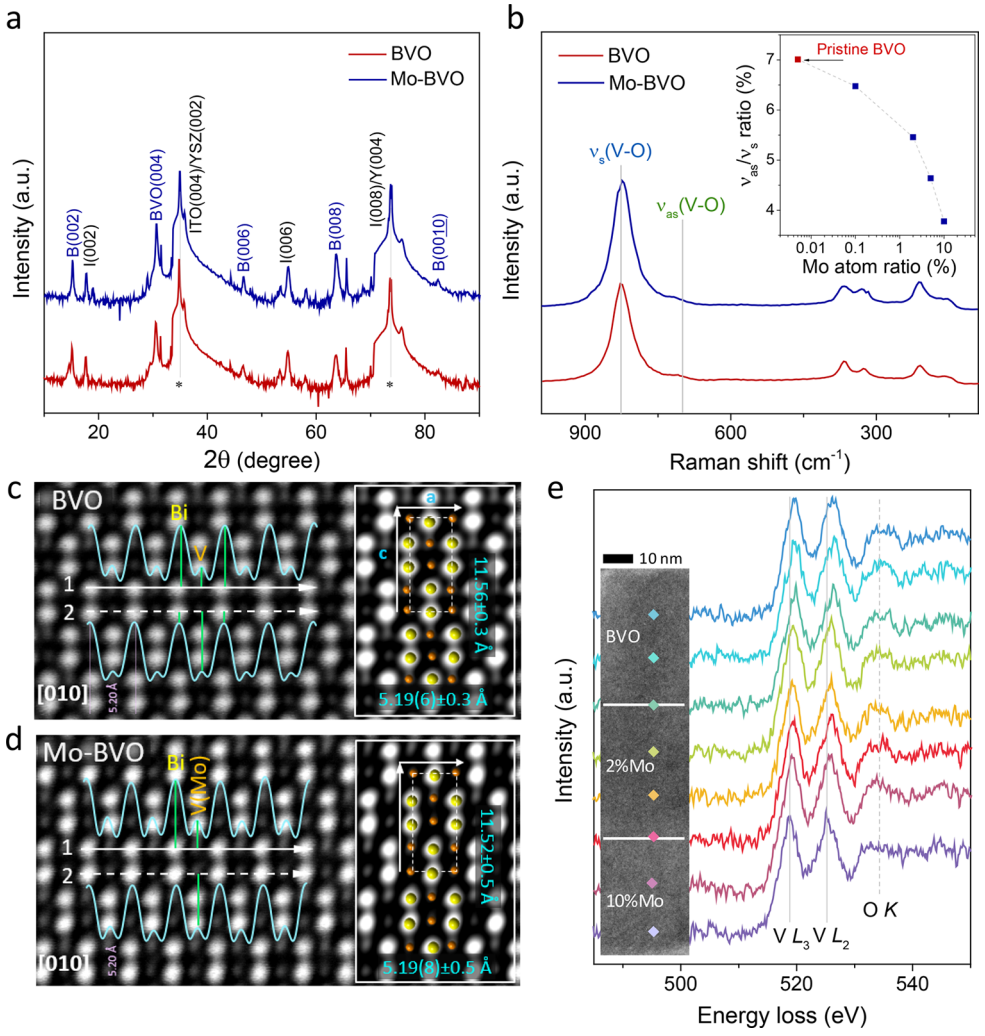


**Figure 2.** (a) $\theta$–$2\theta$ XRD scans of pristine BVO and 2% Mo-BVO films over ITO/YSZ showing *c*-axis-oriented growth. (b) Raman spectra of pristine BVO and 2% Mo-BVO films demonstrating the monoclinic polymorph in pristine BVO and 2% Mo-BVO. The inset shows the ratio of antisymmetric/symmetric Raman bands as a function of Mo dopant concentration. Atomic-resolution HAADF STEM images of (c) pristine BVO and (d) 10% Mo-BVO films identifying the cation position and local lattice structure. (e) High-resolution EELS spectra collected at the V K-edge across a BVO/2% Mo-BVO/10% Mo-BVO trilayer heterostructure with the corresponding cross-sectional TEM image in the inset.

S2b) and energy-dispersive X-ray (EDX) mapping (Figure 1b). The high-resolution STEM image in the high angle annular dark field (HAADF) mode reveals a coherent lattice-matched interface between single-crystalline Mo-BVO and ITO (Figure 1c).

The Mo doping has negligible impact on the optical band gap, which varies over 2.60 ± 0.05 eV for investigated doping levels (Figures 1d and S3). The doping of Mo at 2% or higher slightly lowers the absorption coefficient of BVO films for $\lambda <$ 450 nm. High-resolution X-ray photoelectron spectroscopy (XPS) identifies that the Mo dopants are fully oxidized to $Mo^{6+}$ when the dopant concentration is no larger than 2% (Figure S4a). At higher doping levels, a small amount of $Mo^{4+}$ emerges alongside $Mo^{6+}$ ions. Analysis of V 2p core levels reveals the presence of a small amount of $V^{4+}$ (~3.7%) in pristine BVO, which increases continuously to 4.5–6.0% with incorporated Mo dopants (Figures 1e and S4). As a complementary bulk-sensitive technique,[22] X-ray absorption near-edge structure (XANES) is performed to probe the chemical environment and structural distortion of the entire film. Consistent with the XPS results, the average oxidation state of V is reduced by the Mo doping, as seen from the red shift of V the K-edge in the XANES spectra (Figure 1f).

Structural characterizations reveal that the Mo dopants are substituted into the vanadium sites ($Mo_V$), which introduces slight tetragonal distortion to the parent monoclinic lattice structure of BVO. X-ray diffraction (XRD) results, including the $\theta$–$2\theta$ out-of-plane scans (Figure 2a) and in-plane $\phi$-scans (Figure S5a), confirm the single-crystalline growth of Mo-BVO films in the monoclinic scheelite phase (space group *I*2/*b*, PDF# 01-074-4893).[23] The *c*-axis lattice parameter of Mo-BVO varies within 11.68 ± 0.03 Å for the investigated doping level (Figure S5b), which confirms the phase-pure growth of single-crystalline Mo-BVO. The Mo doping effect on lattice distortion is further analyzed from the Raman bands observed at ~828 and ~710 cm$^{-1}$ (Figure 2b), which are assigned to the symmetric ($\nu_s$) and antisymmetric stretching ($\nu_{as}$) modes of the $VO_4$ tetrahedron, respectively.[24] As *x* increases from 0 to 10% in Mo-BVO, the $\nu_{as}/\nu_s$ ratio diminishes continuously, indicating that the $VO_4$ tetrahedron switches toward a higher tetrahedral symmetry (inset of Figure 2b and Figure S5c).



DOI: 10.1021/acsenergylett.8b01445
ACS Energy Lett. 2018, 3, 2232–2239

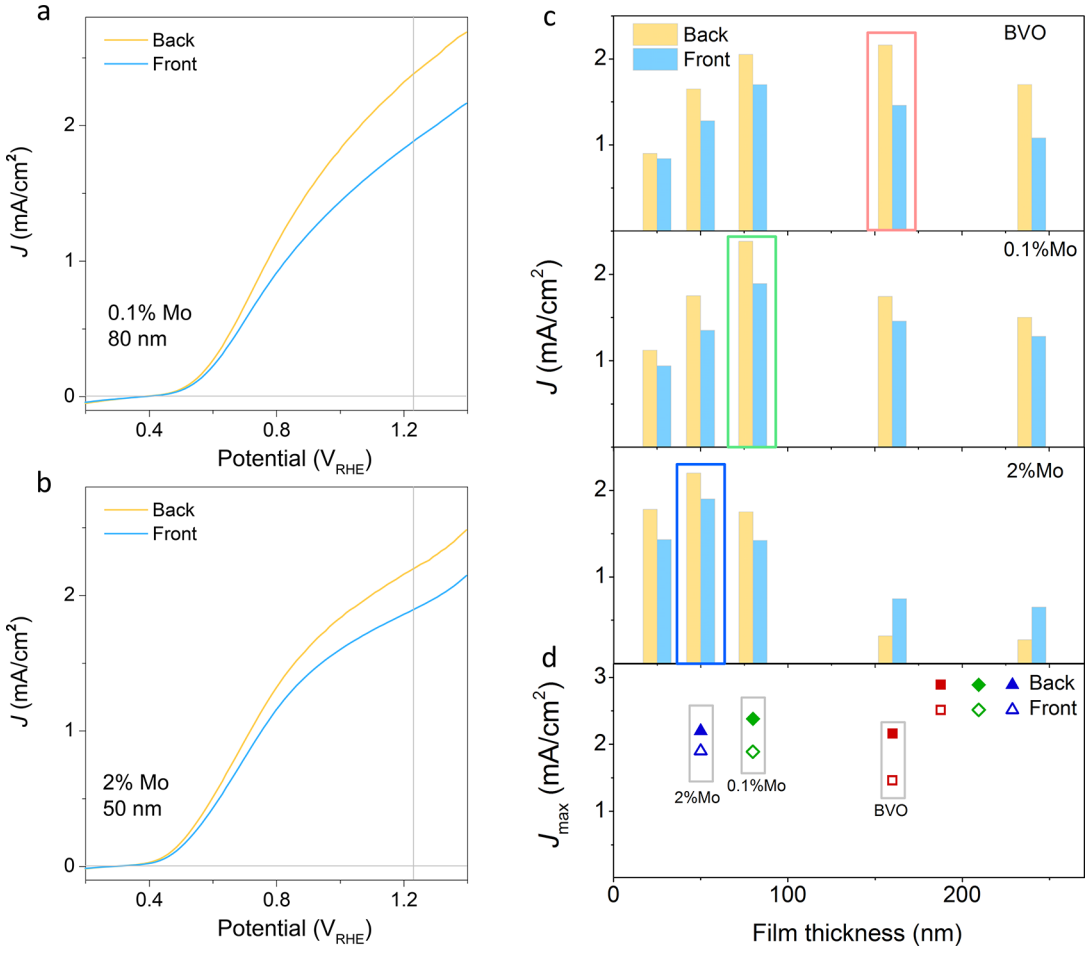


**Figure 3. Photocurrent density versus potential curves of (a) 0.1% Mo-BVO (80 nm thick) and (b) 2% Mo-BVO (50 nm thick) photoanodes under front and back illumination in pH 7.0 phosphate buffer with 1.0 M $Na_2SO_3$. (c) Photocurrent density at 1.23 $V_{RHE}$ of pristine BVO, 0.1% Mo-BVO, and 2% Mo-BVO photoanodes as a function of film thickness and (d) maximum photocurrent for each concentration demonstrating higher photocurrents in Mo-BVO films at significantly thinner thickness than pristine BVO.**

Atomic-resolution HAADF-STEM imaging reveals the same cation arrangement between pristine BVO and Mo-BVO thin films (Figure 2c,d). As seen from the intensity profiles across two neighboring Bi layers, incorporating Mo dopants up to 10% leads to no impurity cluster formation or noticeable change of cation alignment, evidencing the substitutional Mo dopants into the V sites. High-resolution electron energy loss spectroscopy (EELS) is performed around the V L-edge (518−524 eV) to probe the doping effect on the oxidation state variation. A BVO/2% Mo-BVO/10% Mo-BVO trilayer heterostructure is prepared for this analysis, so that the effect of Mo dopant on the V oxidation state can be monitored with pristine BVO as a built-in reference. The V $L_{2,3}$ white lines for Mo-BVO samples feature lower intensities when compared to pristine BVO, which is consistent with the partial replacement of V by Mo (Figure S6). The measured V $L_{2,3}$ spectra at around 517 and 524 eV gradually shift toward lower energy with increasing Mo doping level (Figure 2e), which again demonstrates that the average V oxidation state is reduced in Mo-BVO.

*Tailoring the Photocurrent with Reversed Electron and Hole Collection.* Atomic-scale Mo doping in single-crystalline Mo-BVO thin films exhibits a trade-off effect between the optimization of electron and hole transport. It is noted that the doped Mo-BVO films deliver larger photocurrent than pristine BVO films at significantly thinner thicknesses. A pristine BVO film requires an optimized thickness ($t_{opt}$) of 160 nm to deliver a back-illuminated photocurrent ($J_{back}$) of 2.16 mA/cm$^2$ (Figure S7), while a 0.1% Mo-BVO film is optimized at half of the film thickness, with a larger $J_{back}$ of 2.38 mA/cm$^2$ (Figure 3a). Further increasing the Mo level to 2% reduces the top to an unprecedentedly thin regime (50 nm) (Figure 3b) while maintaining a comparable $J_{back}$ of 2.20 mA/cm$^2$ even with much less photon collection. Such observations are consistent for both sulfite and water oxidations (Figures 3c and S8). In contrast, nanostructured Mo-BVO electrodes in previous reports typically require more than 300 nm thickness for photocurrent optimization,[17−19] which is over 6 times thicker than that of the 2% Mo-BVO film in this study. The incident photon-to-current efficiency (IPCE) and absorbed photon-to-current efficiency (APCE) results are consistent with the photocurrents and thickness dependence. The IPCEs of the 160 nm thick pristine BVO film is slightly smaller to those of the optimized thinner Mo-BVO films, which remain within 42−56% (back illumination) and 32−48% (back illumination) for $\lambda$ < 450 nm (Figure S9). The APCE results include the thickness-dependent absorption and show larger efficiency difference. In the same wavelength region, the thinner Mo-BVO films present 10−20% larger APEC values than those of the pristine BVO film. When the Mo-BVO film



DOI: 10.1021/acsenergylett.8b01445
ACS Energy Lett. 2018, 3, 2232−2239

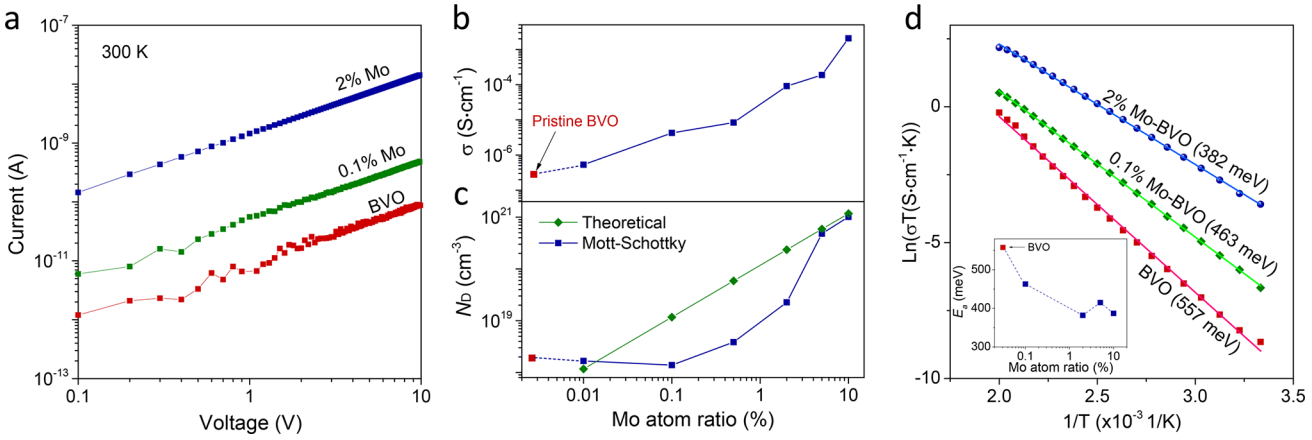


**Figure 4. (a) Current−voltage characteristics of pristine, 0.1% Mo-, and 2% Mo-BVO films showing enhanced conductivity by doping. (b) Film conductivity and (c) donor density of Mo-BVO films as a function of the Mo atom ratio. (d) Conductivity fitting plots of pristine, 0.1% Mo-, and 2% Mo-BVO films based on the small polaron transport model. The inset shows the derived hopping energy in Mo-BVO films as a function of the Mo atom ratio.**

thickness increases to the same value (160 nm) of the pristine BVO, both efficiencies reduce dramatically (Figure S10), in agreement with the photocurrent results.

The observation of larger photocurrent at much thinner Mo-BVO films in Figure 3d (80 nm for 0.1% Mo, 50 nm for 2% Mo) reflects the significance of coordinating both majority and minority carrier transport for optimized device performance. The improved electron transport by Mo doping is very significant in improving the photocurrent even with a shortened hole diffusion length and reduced photon collection. Such results are not expected from Gartner's or Reichmann's models, which suggests that the photocurrent is determined by photohole collection efficiency and is proportional to $\alpha(W + L_p)$, where $\alpha$ is the absorption coefficient, $W$ the depletion width, and $L_p$ the hole diffusion length.[25−27] In contrast, our results reveal higher photocurrents in Mo-BVO films, despite the fact that the Mo doping decreases both $W$ and $L_p$ while having negligible impact on $\alpha$. In particular, the optimized thickness largely reduces from 160 nm in pristine BVO to 50 nm in 2% Mo-BVO in order to match the much reduced $W$ and $L_p$. The $\alpha$ changes less than 10% from pristine BVO to 2% Mo-BVO for band edge absorption. To compensate the photon collection loss in thinner films, the Mo doping must have improved the carrier transport, particularly the electron transport, in a way not considered in these models. Indeed, the charge carrier separation efficiencies ($\eta_{sep}$) are significantly improved from 44.5% (back illumination) and 30.2% (front illumination) in pristine BVO to, respectively, 57.3 and 49.2% in 2% Mo-BVO at their optimized thickness. Overall, Mo doping switches the limiting factor from electron transport in pristine BVO to hole transport in 2% Mo-BVO films, which is confirmed by the reversed photocurrent dependence on the illumination direction for thick films (over 80 nm), as well as the condensed thickness optimization with Mo doping.

*Electronic Characterization and Theoretical Understanding of Small Polaron Transport.* Solid-state electronic characterizations probe the intriguing role of Mo dopants and reveal its synergistic effect in boosting both the donor density and the electron mobility that collectively improve electron transport in single-crystalline Mo-BVO thin films. As determined from the current−voltage ($I$−$V$) characteristics (Figure 4a), the intrinsic electron transport, represented by the in-plane film conductivity ($\sigma_{\parallel}$), is explicitly enhanced by Mo doping. Specifically, $\sigma_{\parallel}$ is doubled from that of pristine BVO ($2.87 \times 10^{-7}$ S·cm$^{-1}$) to 0.01% Mo-BVO ($5.31 \times 10^{-7}$ S·cm$^{-1}$) and is drastically increased by nearly 4 orders of magnitude for 10% Mo-BVO ($2.07 \times 10^{-3}$ S·cm$^{-1}$) (Figure 4b). However, such enhanced film conductivity cannot be supported by only the increased donor density ($N_D$) with Mo dopants. As determined from the Mott−Schottky (MS) analysis, 10% Mo doping enhances the $N_D$ by nearly 3 orders of magnitude (Figure 4c), that is, 1 order of magnitude lower than the improvement level of $\sigma_{\parallel}$. In fact, at lower doping regimes, incorporated Mo dopants may not get fully ionized but compete with intrinsic defects such as native oxygen vacancies. This yields the deviation between MS-derived $N_D$ and the theoretical donor density assuming 100% $Mo_V$ atomic site replacement and full ionization. As such, the contribution of enhanced $N_D$ to the film conductivity can be even less, while the electron mobility must be largely enhanced to account for the improved conductivity.

The improved electron mobility by Mo doping is further identified by the temperature-dependent conductivity results. It is known that the low electron mobility in BVO arises from the formation of small polarons, which are self-trapped due to strong interaction with the surrounding lattice.[28−30] By measuring the temperature-dependent conductivity, we derive the polaron hopping energy ($E_h$) for Mo-BVO films using the $\ln[\sigma(T)T] - 1/T$ linear fit in $\sigma(T) = AT^{-1}\exp\left(-\frac{E_h}{k_B T}\right)$, where $A$ is a constant, $k_B$ the Boltzmann constant, $T$ the temperature, and $E_h$ the hopping activation energy.[31] Interestingly, $E_h$ of Mo-BVO films decreases continuously with increasing Mo dopants from 557 meV for pristine BVO to 382 meV for 2% Mo-BVO and remains at around 400 ± 20 meV for the higher doping level (Figure 4d, inset). Therefore, it is the reduced small polaron hopping barrier that enhances the electron mobility for Mo-BVO and improves the charge carrier separation efficiency.

DFT calculations are performed to gain insights into the Mo doping effect on small polaron transport in BVO. We investigate the reaction pathway to obtain the polaron hopping barriers using the climbing nudged elastic band (CI-NEB) method between two polaronic ground states for pristine BVO and 6.25% Mo-BVO (V replaced with 1:1 neutral Mo atoms, Figure 5a). For both cases, an additional electron is placed at



DOI: 10.1021/acsenergylett.8b01445
ACS Energy Lett. 2018, 3, 2232−2239

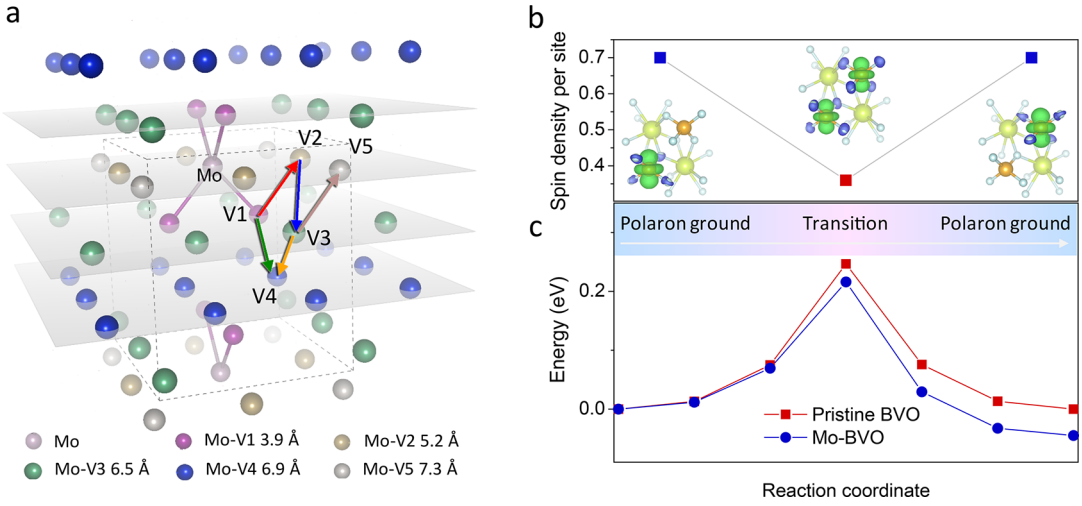


**Figure 5. (a) Schematic small polaron hopping paths in 6.25% Mo-BVO for DFT calculations. Only Mo and V atoms are shown in the schematic structure model. V1−V5 are V positions with different distances to the nearest Mo atom, as listed in the legends. (b) Spin density and (c) average hopping energy barriers in Mo-BVO along the reaction coordination representing one entire small polaron hopping event. The initial state energy of each curve is set to zero. Insets in (b) show the spin-density isosurfaces at a isovalue of 0.002 $e/Å^3$ near the polaron of initial, transition state, and final states along the reaction coordination. The yellow ball denotes Bi ions, orange is for V, and cyan is for O.**

the V site as the extra carrier that forms small polarons, which coincides with the observation of $V^{4+}$ species found in the XPS measurements. The local structures of the polaron in pristine BVO and Mo-BVO are similar: all of the V−O bond lengths in the $VO_4$ tetrahedra containing a small polaron are approximately 0.1 Å longer than those without a polaron.

In pristine BVO, the polaron hopping between nearest neighbors is identical on all sites, for which the computed hopping activation energy is 247 meV (Figure S11a). The spin density plots in Figure 5b identify that the charge is localized on one V atom in both the initial and final polaronic states, while the charge is equally distributed on two sites in the transition state. The local spin is 0.70 $\mu_B$ in the polaronic states and 0.36 $\mu_B$ on both sites in the transition state. The V−O bond lengths in the transition state are also averaged, and both are 0.05 Å longer than those without a polaron. This bond stretching implies strong electron−phonon coupling in this small polaron hopping process. On the other hand, in Mo-BVO, there are several possible inequivalent hopping paths between nearest neighbors in multiple directions, as shown in Figure 5a. We find that the hopping barriers for all hopping paths in Mo-BVO are smaller than those in the pristine BVO, with a lowest barrier of 202 meV for the V3−V5 hopping route (Figure S11b). Due to the limitation of the model, other types of defects such as an oxygen vacancy are not included in the supercell. The absolute value of the calculated hopping activation energy is therefore smaller than the measured values, but the decrease of the polaron hopping energy after Mo-doping can be correctly described nonetheless.

Although the initial and final states are not symmetrical in Mo-BVO, their local spins and structures are still very similar. The local spins of these polaronic states vary between 0.69 and 0.70 $\mu_B$, and the local V−O bond lengths are around 0.09−0.1 Å longer than that without a polaron (Figure S12). The transition states are also similar to that in the pristine state. This indicates that the $VO_4$ tetrahedon is a rigid unit and Mo doping does not influence the local structure of the small polaron significantly. A more drastic change occurs for the polaron hoping barrier at different sites, which suggests the important role of the interaction between the polaron and Mo dopants in affecting electron transport. The positively charged $Mo^{6+}O_4$ unit and negatively charged small polaron $V^{4+}O_4$ unit electrostatically attract each other. On the other hand, both $Mo^{6+}O_4$ and $V^{4+}O_4$ have a larger volume than $V^{5+}O_4$, which forces them to be separated in the crystal for less local structural distortion and a lower energy. Such interaction dominates the electron transport path and provides a lower barrier to hop away from Mo (Figure 5c), therefore facilitating small polaron hopping in Mo-doped BVO. The full oxidation of incorporated Mo dopants is critical to contribute additional electrons to the vanadium sites and to lower the small polaron hopping barrier. For a high doping level (>2%), $Mo^{4+}$ species start to emerge, as seen by the XPS results (Figure S4a), and the hopping barrier does not further decrease (Figure 4d).

In summary, we have discovered the unconventional role of substitutional Mo doping in modulating carrier transport and photocurrents using single-crystalline Mo-doped $BiVO_4$ thin film photoanodes. Through combined solid-state electronic transport and PEC characterizations, it is determined that the improvement of electron transport and charge carrier efficiency in Mo-BVO is largely due to the lowered small polaron hopping barrier. The effect is so significant that higher photocurrent is obtained from significantly thinner Mo-BVO films, despite the much less photon collection. The discovery reflects a clear departure from the conventional models, in which charge carrier separation efficiency never increases toward higher doping. DFT calculations examine the microscopic paths for small polaron transport in Mo-BVO and identify that the lower small polaron hopping barrier by Mo doping is mainly due to minimization of the local lattice expansion caused by both Mo substitution and small polaron formation, in agreement with solid-state electronic characterization results. This study elucidates the important role of extrinsic dopants in boosting the small polaron transport and photocurrent and provides insights into doping engineering for efficient solar water splitting.



DOI: 10.1021/acsenergylett.8b01445
ACS Energy Lett. 2018, 3, 2232−2239

## ■ ASSOCIATED CONTENT

### Supporting Information

The Supporting Information is available free of charge on the ACS Publications website at DOI: 10.1021/acsenergylett.8b01445.

Experimental section, AFM images of Mo-BVO thin films, cross-sectional STEM image and electron diffraction pattern, optical absorption of Mo-BVO films, high-resolution XPS analysis, XRD and Raman characterization, high-resolution EELS analysis, polarization curves under front or back illumination, water oxidation photocurrent dependence on doping level and film thickness, hopping energy barrier calculation, and density of states for the polaron transition (PDF)

## ■ AUTHOR INFORMATION


### Corresponding Author

*E-mail: mzliu@bnl.gov.

### ORCID

Wenrui Zhang: 0000-0002-0223-1924
Danhua Yan: 0000-0003-4112-3018
Yuan Ping: 0000-0002-0123-3389
Mingzhao Liu: 0000-0002-0999-5214


### Notes

The authors declare no competing financial interest.

## ■ ACKNOWLEDGMENTS

This research used resources of the Center for Functional Nanomaterials and the Inner Shell Spectroscopy 8-ID beamline of the National Synchrotron Light Source II, which are U.S. DOE Office of Science User Facilities, and the Scientific Data and Computing Center, a component of the Computational Science Initiative, at Brookhaven National Laboratory under Contract No. DE-SC0012704. J.T. was supported by the DOE BES Early Career Award Program at Brookhaven National Laboratory under Contract DE-SC0012704. Y.P. was supported by National Science Foundation under grant No. DMR-1760260 and Hellman Fellowship. Part of the computer time was provided by the Extreme Science and Engineering Discovery Environment (XSEDE), which is supported by National Science Foundation Grant Number ACI-1548562.[32]

## ■ REFERENCES


(1) Nomura, K.; Ohta, H.; Ueda, K.; Kamiya, T.; Hirano, M.; Hosono, H. Thin-Film Transistor Fabricated in Single-Crystalline Transparent Oxide Semiconductor. *Science* **2003**, *300*, 1269−1272.

(2) Koenraad, P. M.; Flatte, M. E. Single Dopants in Semiconductors. *Nat. Mater.* **2011**, *10*, 91−100.

(3) Zhang, W.; Ramesh, R.; MacManus-Driscoll, J. L.; Wang, H. Multifunctional, Self-Assembled Oxide Nanocomposite Thin Films and Devices. *MRS Bull.* **2015**, *40*, 736−745.

(4) Fan, Y.; Kou, X.; Upadhyaya, P.; Shao, Q.; Pan, L.; Lang, M.; Che, X.; Tang, J.; Montazeri, M.; Murata, K.; et al. Electric-Field Control of Spin−Orbit Torque in a Magnetically Doped Topological Insulator. *Nat. Nanotechnol.* **2016**, *11*, 352−359.

(5) Yuan, M.; Liu, M.; Sargent, E. H. Colloidal Quantum Dot Solids for Solution-Processed Solar Cells. *Nat. Energy* **2016**, *1*, 16016.

(6) Green, M. A.; Bremner, S. P. Energy Conversion Approaches and Materials for High-Efficiency Photovoltaics. *Nat. Mater.* **2017**, *16*, 23−34.

(7) Khan, S. U. M.; Al-Shahry, M.; Ingler, W. B. Efficient Photochemical Water Splitting by a Chemically Modified N-$TiO_2$. *Science* **2002**, *297*, 2243−2245.

(8) Hisatomi, T.; Kubota, J.; Domen, K. Recent Advances in Semiconductors for Photocatalytic and Photoelectrochemical Water Splitting. *Chem. Soc. Rev.* **2014**, *43*, 7520−7535.

(9) Kim, T. W.; Ping, Y.; Galli, G. A.; Choi, K.-S. Simultaneous Enhancements in Photon Absorption and Charge Transport of Bismuth Vanadate Photoanodes for Solar Water Splitting. *Nat. Commun.* **2015**, *6*, 8769.

(10) Abdi, F. F.; Han, L.; Smets, A. H. M.; Zeman, M.; Dam, B.; van de Krol, R. Efficient Solar Water Splitting by Enhanced Charge Separation in a Bismuth Vanadate-Silicon Tandem Photoelectrode. *Nat. Commun.* **2013**, *4*, 2195.

(11) Yin, W.-J.; Wei, S.-H.; Al-Jassim, M. M.; Turner, J.; Yan, Y. Doping Properties of Monoclinic $BiVO_4$ Studied by First-Principles Density-Functional Theory. *Phys. Rev. B: Condens. Matter Mater. Phys.* **2011**, *83*, 155102.

(12) Pilli, S. K.; Furtak, T. E.; Brown, L. D.; Deutsch, T. G.; Turner, J. A.; Herring, A. M. Cobalt-Phosphate (Co-Pi) Catalyst Modified Mo-Doped $BiVO_4$ Photoelectrodes for Solar Water Oxidation. *Energy Environ. Sci.* **2011**, *4*, 5028−5034.

(13) Ye, H.; Park, H. S.; Bard, A. J. Screening of Electrocatalysts for Photoelectrochemical Water Oxidation on W-Doped $BiVO_4$ Photocatalysts by Scanning Electrochemical Microscopy. *J. Phys. Chem. C* **2011**, *115*, 12464−12470.

(14) Park, Y.; McDonald, K. J.; Choi, K.-S. Progress in Bismuth Vanadate Photoanodes for Use in Solar Water Oxidation. *Chem. Soc. Rev.* **2013**, *42*, 2321−2337.

(15) Zhang, W.; Yan, D.; Tong, X.; Liu, M. Ultrathin Lutetium Oxide Film as an Epitaxial Hole-Blocking Layer for Crystalline Bismuth Vanadate Water Splitting Photoanodes. *Adv. Funct. Mater.* **2018**, *28*, 1705512.

(16) Kim, M.-W.; Kim, K.; Ohm, T. Y.; Joshi, B.; Samuel, E.; Swihart, M. T.; Yoon, H.; Park, H.; Yoon, S. S. Mo-Doped $BiVO_4$ Nanotextured Pillars as Efficient Photoanodes for Solar Water Splitting. *J. Alloys Compd.* **2017**, *726*, 1138−1146.

(17) Luo, W.; Yang, Z.; Li, Z.; Zhang, J.; Liu, J.; Zhao, Z.; Wang, Z.; Yan, S.; Yu, T.; Zou, Z. Solar Hydrogen Generation from Seawater with a Modified $BiVO_4$ Photoanode. *Energy Environ. Sci.* **2011**, *4*, 4046−4051.

(18) Chen, L.; Toma, F. M.; Cooper, J. K.; Lyon, A.; Lin, Y.; Sharp, I. D.; Ager, J. W. Mo-Doped $BiVO_4$ Photoanodes Synthesized by Reactive Sputtering. *ChemSusChem* **2015**, *8*, 1066−1071.

(19) Seabold, J. A.; Zhu, K.; Neale, N. R. Efficient Solar Photoelectrolysis by Nanoporous Mo:$BiVO_4$ through Controlled Electron Transport. *Phys. Chem. Chem. Phys.* **2014**, *16*, 1121−1131.

(20) Yao, W.; Iwai, H.; Ye, J. Effects of Molybdenum Substitution on the Photocatalytic Behavior of $BiVO_4$. *Dalton Trans.* **2008**, 1426−1430.

(21) Guo, W.; Ward, T. L.; Porter, C.; Datye, A. K. Phase Content and Particle Morphology of Bi−Mo−V−O Powders Produced by Aerosol Pyrolysis. *Mater. Res. Bull.* **2005**, *40*, 1371−1387.

(22) Horrocks, G. A.; Braham, E. J.; Liang, Y.; De Jesus, L. R.; Jude, J.; Velázquez, J. M.; Prendergast, D.; Banerjee, S. Vanadium K-Edge X-Ray Absorption Spectroscopy as a Probe of the Heterogeneous Lithiation of $V_2O_5$: First-Principles Modeling and Principal Component Analysis. *J. Phys. Chem. C* **2016**, *120*, 23922−23932.

(23) Sleight, A. W.; Chen, H. y.; Ferretti, A.; Cox, D. E. Crystal Growth and Structure of $BiVO_4$. *Mater. Res. Bull.* **1979**, *14*, 1571−1581.

(24) Hardcastle, F. D.; Wachs, I. E. Determination of Vanadium-Oxygen Bond Distances and Bond Orders by Raman Spectroscopy. *J. Phys. Chem.* **1991**, *95*, 5031−5041.

(25) Butler, M. A.; Ginley, D. S. Principles of Photoelectrochemical, Solar Energy Conversion. *J. Mater. Sci.* **1980**, *15*, 1−19.

(26) Gärtner, W. W. Depletion-Layer Photoeffects in Semiconductors. *Phys. Rev.* **1959**, *116*, 84−87.




DOI: 10.1021/acsenergylett.8b01445
*ACS Energy Lett.* 2018, 3, 2232−2239

(27) Reichman, J. The Current-Voltage Characteristics of Semiconductor-Electrolyte Junction Photovoltaic Cells. *Appl. Phys. Lett.* **1980**, *36*, 574−577.
(28) Rettie, A. J. E.; Chemelewski, W. D.; Emin, D.; Mullins, C. B. Unravelling Small-Polaron Transport in Metal Oxide Photoelectrodes. *J. Phys. Chem. Lett.* **2016**, *7*, 471−479.
(29) Smart, T.; Ping, Y. Effect of Defects on the Small Polaron Formation and Transport Properties of Hematite from First-Principles Calculations. *J. Phys.: Condens. Matter* **2017**, *29*, 394006.
(30) Zhang, W.; Yan, D.; Li, J.; Wu, Q.; Cen, J.; Zhang, L.; Orlov, A.; Xin, H.; Tao, J.; Liu, M. Anomalous Conductivity Tailored by Domain-Boundary Transport in Crystalline Bismuth Vanadate Photoanodes. *Chem. Mater.* **2018**, *30*, 1677−1685.
(31) Austin, I. G.; Mott, N. F. Polarons in Crystalline and Non-Crystalline Materials. *Adv. Phys.* **1969**, *18*, 41−102.
(32) Towns, J.; Cockerill, T.; Dahan, M.; Foster, I.; Gaither, K.; Grimshaw, A.; Hazlewood, V.; Lathrop, S.; Lifka, D.; Peterson, G. D.; et al. Xsede: Accelerating Scientific Discovery. *Comput. Sci. Eng.* **2014**, *16*, 62−74.



DOI: 10.1021/acsenergylett.8b01445
*ACS Energy Lett.* 2018, 3, 2232−2239